Characterization of a semidiurnal eastward-propagating tide at high northern latitudes with Mars Global Surveyor electron density profiles

K. L. Cahoy,[1] D. P. Hinson,[1] and G. L. Tyler[1]

[1]   Apparent phase velocities of zonal structure, estimated from Mars Global Surveyor (MGS) electron density profiles, are used to identify and characterize SE1, the semidiurnal eastward-propagating tide with zonal wave number one, at high northern latitudes during the summer of Mars Year 26. SE1 shows impressive phase stability with altitude, season, and local time. SE1 maintains a presence at amplitudes between 5 and 15% of the zonal mean at 125 ± 10 km altitude for most of the summer season. Further analyses using MGS electron density profiles will contribute to the identification and characterization of nonmigrating tides in the upper atmosphere of Mars. **Citation:** Cahoy, K. L., D. P. Hinson, and G. L. Tyler (2007), Characterization of a semidiurnal eastward-propagating tide at high northern latitudes with Mars Global Surveyor electron density profiles, *Geophys. Res. Lett.*, *34*, L15201, doi:10.1029/2007GL030449.

1. Introduction

[2]   This paper reports new observations consistent with SE1, the semidiurnal eastward-propagating tide with zonal wave number one on Mars. We characterize its effect on ionospheric structure at high northern latitudes through analysis of electron density profiles obtained with MGS during northern summer of Mars Year 26 (MY26). *Clancy et al.* [2000] defines Mars Year 1 as commencing on April 11, 1955. The data in this work are from November 1, 2002–June 4, 2003, $L_S = 89$–$200°$, where L_S is the areocentric longitude of the Sun and $L_S = 0°$ corresponds to vernal equinox in the northern hemisphere.

[3]   On Mars, the structure of the primary electron density peak is controlled by local photochemistry, and the altitude at which it forms depends on the path length of solar EUV radiation through the underlying neutral atmosphere [*Bougher et al.*, 2001]. Mars lacks an appreciable internal magnetic field, and the influence of crustal magnetic fields is weak at the high northern latitudes considered in this work (60–$85°$N) [*Krymskii et al.*, 2003]. Thermal tides strongly affect the zonal structure of the neutral atmosphere at ionospheric altitudes, as observed by the accelerometer during MGS aerobraking [e.g., *Forbes and Hagan*, 2000; *Forbes et al.*, 2002; *Wilson*, 2002; *Withers et al.*, 2003]. The response of the ionosphere to tidal forcing is also apparent in radio occultation measurements of electron density from MGS [*Bougher et al.*, 2001; *Bougher et al.*, 2004; *Cahoy et al.*, 2006]. The observed zonal variations of electron density arise primarily from the vertical displacement of the ionosphere that results from tidal modulation of neutral density.

[4]   This work characterizes zonal structure with observed wave number $k = 3$ in radio occultation measurements of electron density. We subdivide the MY26 data set into seasonal slices, and calculate the amplitude and phase of zonal structure with $k = 3$ for each slice. The calculated phases are fairly stable with season, and their variation appears to be controlled by the change in local time across the data set. We can, therefore, take advantage of the local time progression of the measurements from 04:00–14:00 to estimate the apparent phase velocity of the $k = 3$ structure. The resulting $\sim 10°$ hr^{-1} apparent phase velocity corresponds to that expected for SE1. We also present the seasonal variation of electron density amplitude (up to 15% of the zonal mean) and phase associated with SE1. This work supports previous measurements and numerical simulations suggesting SE1 as a contributor to observed $k = 3$ structure in the upper atmosphere of Mars, particularly at altitudes relevant to aerobraking [*Bougher et al.*, 2001; *Forbes et al.*, 2002; *Wilson*, 2002; *Withers et al.*, 2003; *Bougher et al.*, 2004; *Angelats i Coll et al.*, 2004; *Cahoy et al.*, 2006]. We extend the characterization of SE1 to a larger altitude range and a ten hour span of local time through the northern summer of MY26.

2. Nonmigrating Tides

[5]   Nonmigrating tides result from interaction between solar-locked migrating tides and planetary-scale forcing, such as that caused by topographic asymmetry [*Zurek*, 1976; *Wilson and Hamilton*, 1996; *Forbes and Hagan*, 2000; *Forbes et al.*, 2002; *Withers et al.*, 2003]. At a fixed latitude, θ, and height, z, both migrating and nonmigrating tides can be represented as a variation in number density, n, about the zonal mean of the form:

$$n_{\sigma,s} = A_{\sigma,s} \cos(\sigma \Omega t + s\lambda - \psi_{\sigma,s}) \quad (1)$$

where A is amplitude, ψ is phase, λ is longitude, t is time in sols, $\Omega = 2\pi \text{ sol}^{-1}$ is the planetary rotation rate, σ is the temporal frequency of the wave ($\sigma = 1$ is diurnal, $\sigma = 2$ is semidiurnal), and $s = 0$, ± 1, ± 2, $\pm 3 \ldots$ is the zonal wave number. For example, $s = +1$ is westward wave one, and $s = -1$ is eastward wave one. In this reference frame, the phase velocity is $-\sigma\Omega/s$.

3. Tides at Fixed Local Time

[6]   Radio occultation measurements made by Mars Global Surveyor provide the profiles of electron density for MY26

---

[1]Department of Electrical Engineering, Stanford University, Stanford, California, USA.
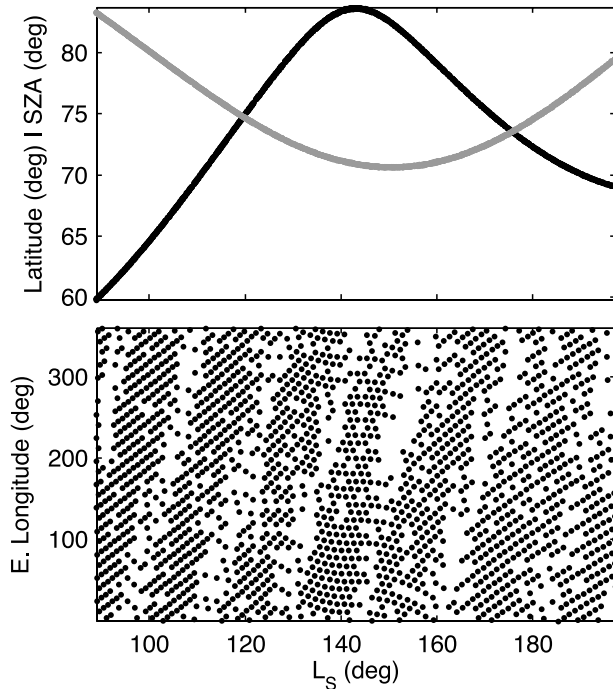
Figure 1. The distribution of 1805 MGS electron density profiles from Mars Year 26 used in this analysis. (top) Latitude (black curve) and solar zenith angle (gray curve) vary with areocentric longitude of the sun, or season, L_S. (bottom) The zonal sampling with season; each dot represents a profile from $100-170$ km.

used in this work, with sampling shown in detail in Figure 1 [*Hinson et al.*, 1999; *Bougher et al.*, 2001]. Over the entire data set, latitude remains within a $25°$ band from $60-85°$N (Figure 1, black line) with solar zenith angle (SZA) in the range of $70-85°$ (Figure 1, gray line). The sample spacing in longitude is about $30°$, with several gaps. The vertical ordinate of the profiles is altitude above a reference areoid with mean equatorial radius 3,396 km.

[7] We interpolate the data in season and longitude using the method of *Randel and Wu* [2005], a Gaussian-weighted average with standard deviations $D = 10°$ of longitude and $T = 4°$ of L_S. We then subdivide the data, remove the zonal mean, and perform zonal decomposition on separate slices of $4°$ L_S, or roughly 7 sols. The local time and latitude of the measurements within each slice are essentially constant. Local time increases monotonically across the data set. We modify the equation representing tides at fixed latitude to the local time reference frame using $t = t_{LT} - \lambda/2\pi$:

$$n_{\sigma,s} = A_{\sigma,s} \cos\left(\sigma\Omega t_{LT} + (s - \sigma)\lambda - \psi_{\sigma,s}\right) \tag{2}$$

The apparent phase velocity with respect to local time is:

$$v_p = \frac{-\sigma\Omega}{s - \sigma} \tag{3}$$

For fixed local time, the equation representing tides at fixed latitude can be further simplified by setting $k = |s - \sigma|$ and consolidating the now-constant $\sigma \Omega t_{LT}$ into a new phase term, λ_k:

$$n_k = A_k \cos[k(\lambda - \lambda_k)] \tag{4}$$

where

$$\lambda_k = \frac{\psi_{\sigma,s} - \sigma\Omega t_{LT}}{(s - \sigma)} \tag{5}$$

It is also convenient to define $\phi_k = k\lambda_k$, since the least-squares wave decomposition used in this work solves for A_k and ϕ_k. In observations at fixed local time, multiple combinations of σ and s yield the same value of k. For example, SE1 would appear as $k = |-1 - 2| = 3$, as would any other wave with $|s - \sigma| = 3$, such as the zonally symmetric terdiurnal wave ($\sigma = 3$, $s = 0$).

4. Apparent Phase Velocity

[8] This MY26 data set comprises twenty-eight slices of $4°$ in L_S at different fixed t_{LT}. If λ_k remains fairly stable with season, latitude, and SZA across several of the slices, we can use its progression in local time to estimate the apparent phase velocity, v_p:

$$\frac{d\lambda_k}{dt_{LT}} = \frac{1}{k}\frac{d\phi_k}{dt_{LT}} = \frac{-\sigma\Omega}{(s - \sigma)} = v_p \tag{6}$$

If $d\phi_k/dt_{LT}$ is determined to be positive, $(s - \sigma)$ must be negative. Conversely, if $d\phi_k/dt_{LT}$ is negative, $(s - \sigma)$ must be positive. Each combination of σ and s yield a different value for v_p, as shown in Table 1 for $k = 3$. The estimate of v_p can therefore be used, in principle, to determine the σ and s of the dominant contributor.

5. Wave Decomposition Result

[9] We apply the same method of analysis used by *Cahoy et al.* [2006], using weighted least squares to decompose the zonal structure at fixed altitude. The sample spacing in longitude is $\sim 30°$, allowing consideration of zonal variation for $k = 1-6$ without aliasing. Figure 2 (top) shows a sample decomposition for $k = 1-6$ for one $4°$ L_S slice, from $L_S = 99-103°$ at 125 km. The data exhibit well defined zonal variation, and the spacing of the crests and troughs implies the presence of structure with $k > 4$.

[10] Figures 2 (middle) and 2 (bottom) show the corresponding individual amplitudes, A_k, and phases, ϕ_k over the entire altitude range for this slice of data. The amplitudes for A_2-A_5 appear strongest for this subset of data. We note that the radio occultation measurement senses the density of charged particles. This should be kept in mind when viewing the resulting amplitudes and phases, as the method is most sensitive at 125 km, just below the electron density peak, where electron density, n_e, and its gradient are strongest [*Cahoy et al.*, 2006].

[11] Here, we focus primarily on $k = 3$. The phase for $k = 3$ increases fairly linearly with altitude in the eastward direction. There are some $5-10$ km scale vertical regions with variation, but overall, the vertical phase progression is quite stable for this subset of data. These wave decompo-

Table 1. Apparent Phase Velocities for $k = 3$ in deg. hr^{-1}

	$\sigma = 1$	$\sigma = 1$	$\sigma = 2$	$\sigma = 2$	$\sigma = 3$	$\sigma = 3$	$\sigma = 4$	$\sigma = 4$
s	-2	4	-1	5	0	6	1	7
v_p	5	-5	10	-10	15	-15	20	-20

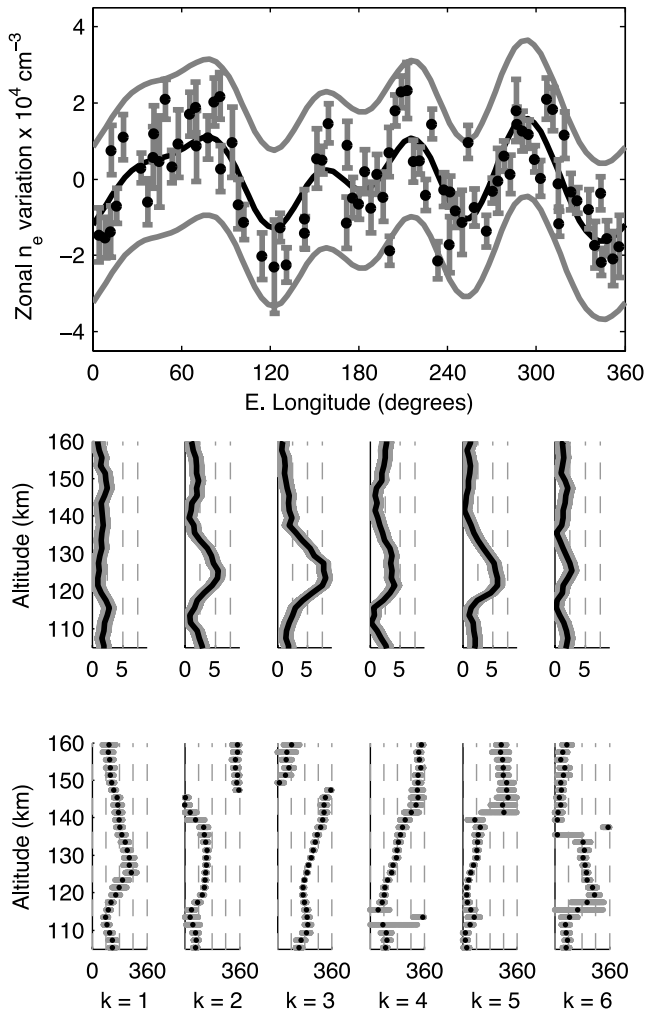**Figure 2.** (top) Example of wave structure at 125 km for a 4° L_S subset of data, from $L_S = 99-103°$ of MY26. The black circles are the measured values with ±1 standard deviation experimental error bars. The black line is the least-squares fit for $k = 1-6$. The gray lines are a 95% confidence envelope on the fit. Corresponding (middle) amplitudes (A_{1-6}) and (bottom) phases (ϕ_{1-6}) shown from 105–160 km. Amplitude shown in units of 10^3 cm^{-3} and phase in degrees East longitude. Vertical dashed guidelines in amplitude map to 2.5, 5, and 7.5 × 10^3 cm^{-3}. Vertical dashed guidelines in phase correspond to 90° spacing. Both shown with ±1 standard deviation gray envelopes. Phase data are shown with 2 km vertical spacing (dots) to clarify wraps in phase.

sition results for a single slice in the MY26 northern summer data set give a sense of the variety and level of detail embedded within the extensive catalog of radio occultation measurements performed by MGS.

6. Result for the Full MY26 Season

[12] We performed the same decomposition shown for a single slice in Figure 2 for twenty-seven additional 4° L_S slices across the MY26 data set. The composite results for $k = 3$ are shown as A_3 and ϕ_3 vs. L_S in Figure 3.

[13] The $k = 3$ amplitude remains strong, from 5–15% of the zonal mean, at 125 ± 10 km for nearly the entire summer season. We further observe an increase in amplitude around 105 km, possibly associated with the lower secondary peak in electron density near that altitude. Early in the summer season (and at earlier local time), there also appears to be notable strength in amplitude (up to 7.5%) at high altitudes (160 km). This also could be attributed to higher SZA, which results in a relatively small electron density. Another potential cause of variation is the slowly drifting latitude (Figure 1).

[14] The composite phase results for $k = 3$ for the entire MY26 summer season are shown in Figure 3 (middle) together with monotonically increasing local time (Figure 3, bottom) versus season. Considering that phase was solved for at each altitude independently, the stability of ϕ_3 with
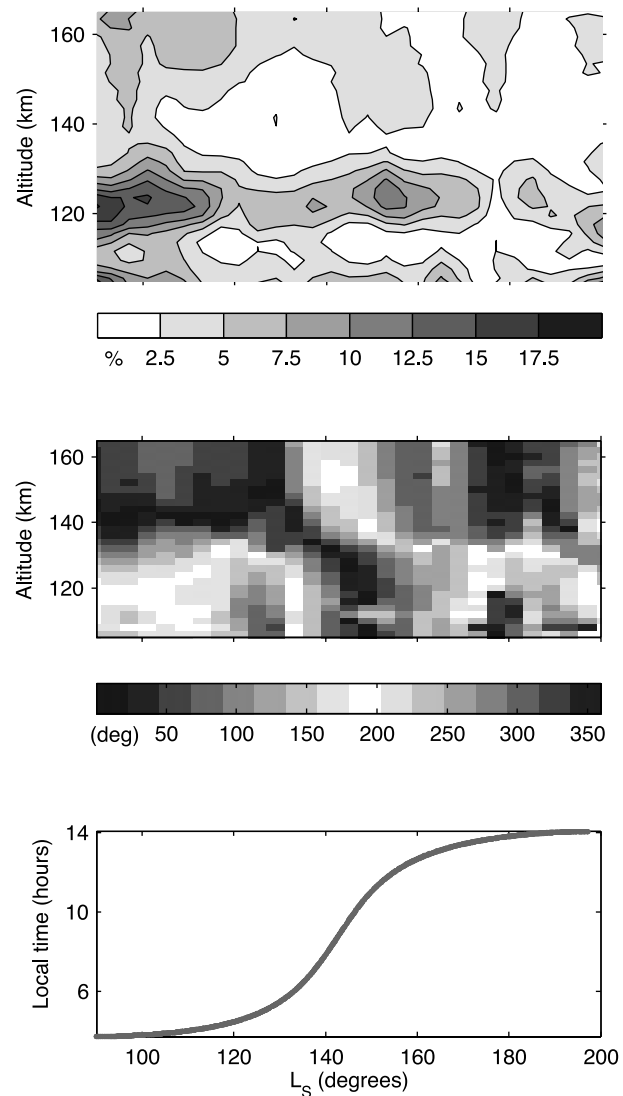

Figure 3. (top) Amplitude for $k = 3$ shown with season and altitude. Amplitude is shown as percent variation about the zonal mean. Contour intervals are 2.5%. (middle) Phase for $k = 3$ shown with season and altitude. The phase color map is circular, in 22.5° steps. Figure 2 for ϕ_3 provides one absolute reference. (bottom) Local time vs. season.
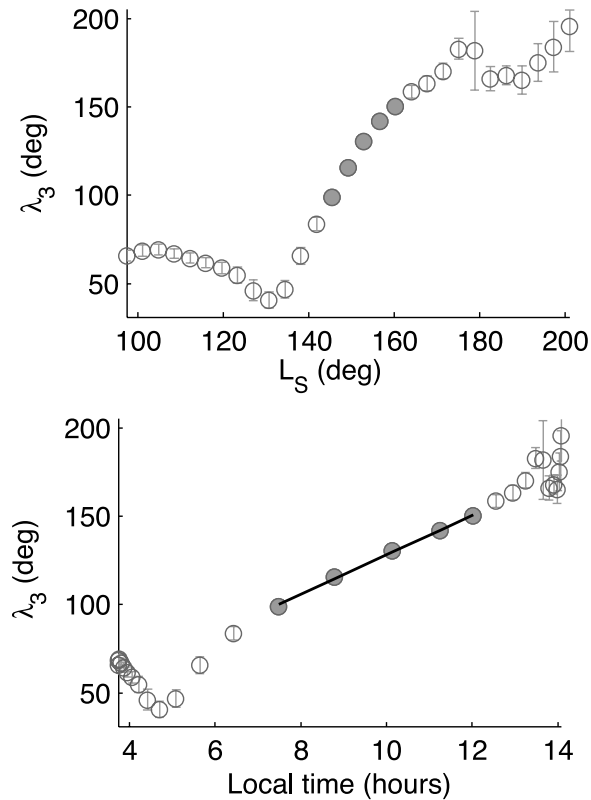
Figure 4. (top) λ_3 at 125 km (circles) versus L_S. Error bars represent ±1 standard deviation. (bottom) λ_3 as for Figure 4 (top), but shown versus local time. The slope of the black line through the solid gray circles is the estimated v_p. For this example at 125 km, $v_p = 11°$ hr^{-1}.

both altitude and season is remarkable, particularly in the morning (earlier L_S). The phase change with season appears, at most altitudes, to be controlled by the change in local time, making ϕ_3 a good candidate for apparent phase velocity estimation.

7. Phase Stability

[15] Figure 4 sharpens the view of phase stability with both local time and season at an altitude of 125 km. The progression of phase for $k = 3$ is shown with season as $\lambda_k = \phi_k/k$. The change in phase is controlled by the change in local time (compare Figure 4, top, to Figure 3, bottom). The solid circles represent the five values selected for use in estimating the apparent phase velocity. These were chosen based on their small error bars and their location on the steepest slope of the local time curve. We note that although Figure 4 is representative of most altitudes for $k = 3$ in this data set, it is not representative of the stability for all k, nor is it necessarily representative of $k = 3$ for other seasons or local times than those discussed here.

8. Phase Velocity Result

[16] We estimate an apparent phase velocity of $11°$ hr^{-1} for observed $k = 3$ as shown in Figure 4 (bottom), using a weighted least-squares fit with the phase errors as weights.

In Figure 5, we address both how the estimated v_p behaves with altitude, and whether or not the estimate yields a clear solution for (σ, s) among the possibilities presented in Table 1. Each × in Figure 5 represents an estimated apparent phase velocity, while the gray envelope marks ±1 standard deviation confidence in the goodness of the linear fit. The black vertical lines directly map to the possible apparent phase velocities shown in Table 1. For altitudes between 120–160 km, SE1 appears to be the closest candidate. At higher altitudes, where there is less confidence in the fit and stability, the estimated phase velocities drift toward nonmigrating candidate DE2 ($\sigma = 1$, $s = -2$) with $v_p = 5°$ hr^{-1}. At ~115 km, there is a single outlier on the zonally symmetric terdiurnal line ($\sigma = 3$, $s = 0$). This result seems physically unlikely within such a narrow altitude range. Such outliers are likely due to a combination of weak amplitude at $k = 3$, errors in the initial phase calculation, contribution from other modes, or variation with season or latitude.

9. Conclusion

[17] These results corroborate earlier studies that showed behavior consistent with semidiurnal frequency in MGS aerobraking and electron density data and that suggested SE1 as a strong candidate [Bougher et al., 2001; Withers et al., 2003]. Numerical simulations have also shown SE1 as a contributor to $k = 3$ structure observed in both MGS aerobraking neutral density and radio occultation electron density measurements during late spring in the Northern Hemisphere [cf. Wilson, 2002, Figure 3; Bougher et al., 2004, Figure 10; Angelats i Coll et al., 2004, Figure 5]. These simulations are all slightly earlier in L_S than the MY26 data presented here. Simulation results supporting SE1 were also reported at a later season ($L_S = 270°$) [Forbes et al., 2002, Figure 6]. Our results extend this work by providing direct experimental characterization of SE1 at high northern latitudes for the full summer season of MY26. SE1 shows impressive phase stability with altitude, season and local time, as well as maintaining a presence at amplitudes between 5 and 15% of the electron density zonal mean at 125 ± 10 km altitude. Further analyses using MGS electron density profiles will contribute to the iden-
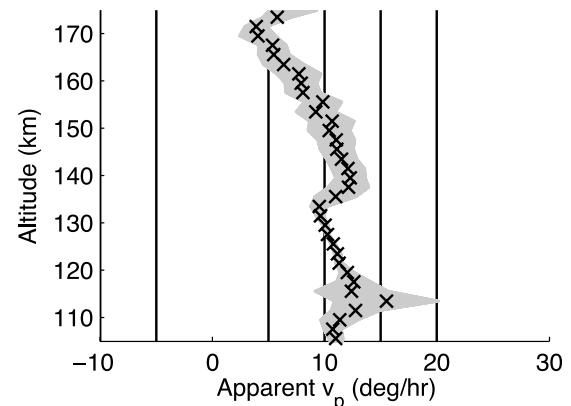

Figure 5. Estimated apparent phase velocities for $k = 3$ vs. altitude. Vertical black lines compare the estimates with predictions in Table 1.

tification and characterization of nonmigrating tides in the upper atmosphere of Mars.

References

Angelats i Coll, M., F. Forget, M. A. López-Valverde, P. L. Read, and S. R. Lewis (2004), Upper atmosphere of Mars up to 120 km: Mars Global Surveyor accelerometer data analysis with the LMD general circulation model, *J. Geophys. Res.*, *109*, E01011, doi:10.1029/2003JE002163.

Bougher, S. W., S. Engel, D. P. Hinson, and J. M. Forbes (2001), Mars Global Surveyor Radio Science electron density profiles: Neutral atmosphere implications, *Geophys. Res. Lett.*, *28*, 3091–3094.

Bougher, S. W., S. Engel, D. P. Hinson, and J. R. Murphy (2004), MGS Radio Science electron density profiles: Interannual variability and implications for the Martian neutral atmosphere, *J. Geophys. Res.*, *109*, E03010, doi:10.1029/2003JE002154.

Cahoy, K. L., D. P. Hinson, and G. L. Tyler (2006), Radio science measurements of atmospheric refractivity with Mars Global Surveyor, *J. Geophys. Res.*, *111*, E05003, doi:10.1029/2005JE002634.

Clancy, R. T., B. J. Sandor, M. J. Wolff, P. R. Christensen, M. D. Smith, J. C. Pearl, B. J. Conrath, and R. J. Wilson (2000), An intercomparison of ground-based millimeter, MGS TES, and Viking atmospheric temperature measurements: Seasonal and interannual variability of temperatures and dust loading in the global Mars atmosphere, *J. Geophys. Res.*, *105*, 9553–9571, doi:10.1029/1999JE001089.

Forbes, J. M., and M. E. Hagan (2000), Diurnal Kelvin wave in the atmosphere of Mars: Towards an understanding of 'stationary' density structures observed by the MGS accelerometer, *Geophys. Res. Lett.*, *27*, 3564–3566, doi:10.1029/2000GL011850.

Forbes, J. M., A. F. C. Bridger, S. W. Bougher, M. E. Hagan, J. L. Hollingsworth, G. M. Keating, and J. Murphy (2002), Nonmigrating tides in the thermosphere of Mars, *J. Geophys. Res.*, *107*(E11), 5113, doi:10.1029/2001JE001582.

Hinson, D. P., R. A. Simpson, J. D. Twicken, G. L. Tyler, and F. M. Flasar (1999), Initial results from radio occultation measurements with Mars Global Surveyor, *J. Geophys. Res.*, *104*, 26,997–27,012, doi:10.1029/1999JE001069.

Krymskii, A. M., T. K. Breus, N. F. Ness, D. P. Hinson, and D. I. Bojkov (2003), Effect of crustal magnetic fields on the near terminator ionosphere at Mars: Comparison of in situ magnetic field measurements with the data of radio science experiments on board Mars Global Surveyor, *J. Geophys. Res.*, *108*(A12), 1431, doi:10.1029/2002JA009662.

Randel, W. J., and F. Wu (2005), Kelvin wave variability near the equatorial tropopause observed in GPS radio occultation measurements, *J. Geophys. Res.*, *110*, D03102, doi:10.1029/2004JD005006.

Wilson, R. J. (2002), Evidence for nonmigrating thermal tides in the Mars upper atmosphere from the Mars Global Surveyor Accelerometer Experiment, *Geophys. Res. Lett.*, *29*(7), 1120, doi:10.1029/2001GL013975.

Wilson, R. J., and K. Hamilton (1996), Comprehensive model simulation of thermal tides in the Martian atmosphere, *J. Atmos. Sci.*, *53*, 1290–1326.

Withers, P., S. W. Bougher, and G. M. Keating (2003), The effects of topographically-controlled thermal tides in the Martian upper atmosphere as seen by the MGS accelerometer, *Icarus*, *164*, 14–32, doi:10.1016/S0019-1035(03)00135-0.

Zurek, R. W. (1976), Diurnal tide in the Martian atmosphere, *J. Atmos. Sci.*, *33*, 321–337.

———————————

K. L. Cahoy, D. P. Hinson, and G. L. Tyler, Department of Electrical Engineering, Stanford University, STAR Lab, 350 Serra Mall, Stanford, CA 94305, USA. (kcahoy@stanford.edu)